



# Deciphering the role of the MALT1–RC3H1 axis in regulating GPX4 protein stability

Jun Wang<sup>a,1</sup>, Long Liao<sup>a,1</sup>, Beiping Miao<sup>a,b,1</sup> , Bo Yang<sup>c,1</sup>, Botai Li<sup>d</sup>, Xuhui Ma<sup>a,e</sup>, Annika Fitz<sup>b</sup>, Shanshan Wu<sup>a</sup>, Jia He<sup>f</sup>, Qianqian Zhang<sup>g</sup>, Shuyi Ji<sup>h</sup>, Guangzhi Jin<sup>i</sup>, Jianming Zhang<sup>j</sup>, Ying Cao<sup>a</sup>, Hui Wang<sup>a</sup>, Wenxin Qin<sup>a,2</sup>, Chong Sun<sup>b,2</sup>, René Bernards<sup>a,k,2</sup> , and Cun Wang<sup>a,2</sup>

Affiliations are included on p. 11.

Contributed by René Bernards; received September 24, 2024; accepted November 25, 2024; reviewed by Sidong Huang and Eli Pikarsky

**Ferroptosis**, a unique form of iron-dependent cell death triggered by lipid peroxidation accumulation, holds great promise for cancer therapy. Despite the crucial role of GPX4 in regulating ferroptosis, our understanding of GPX4 protein regulation remains limited. Through FACS-based genome-wide CRISPR screening, we identified MALT1 as a regulator of GPX4 protein. Inhibition of MALT1 expression enhances GPX4 ubiquitination-mediated degradation by up-regulating the E3 ubiquitin ligase RC3H1. Using both rescue assays and functional genetic screening, we demonstrate that pharmacologically targeting MALT1 triggers ferroptosis in liver cancer cells. Moreover, we show that targeting MALT1 synergizes with sorafenib or regorafenib to induce ferroptosis across multiple cancer types. These findings elucidate the modulatory effects of the MALT1–RC3H1 axis on GPX4 stability, revealing a molecular mechanism that could be exploited to induce ferroptosis for cancer therapy.

ferroptosis | GPX4 | MALT1 | liver cancer

Ferroptosis is a form of regulated cell death that is characterized by the accumulation of iron-dependent lipid peroxidation and subsequent membrane damage (1, 2). In recent years, there has been growing interest in studying the role of ferroptosis in tumorigenesis and cancer therapy (3, 4). Certain types of cancer cells, characterized by specific metabolic features, genetic mutations, or imbalanced ferroptosis defense mechanisms, exhibit heightened susceptibility to ferroptosis (5, 6). These findings have sparked interest in exploiting ferroptosis as a potential therapeutic strategy for cancer treatment.

Glutathione peroxidase 4 (GPX4) plays a crucial role in regulating ferroptosis by reducing lipid hydroperoxides and protecting cells from oxidative stress (3). GPX4 employs glutathione (GSH) as a cofactor to transform harmful lipid hydroperoxides (L-OOH) into nontoxic lipid alcohols (L-OH) (3). Targeting GPX4 to promote ferroptosis has been proposed as a promising cancer treatment strategy. However, the development of effective GPX4 inhibitors has proven challenging because it lacks a conventional drug-binding site and relies on a nucleophilic selenocysteine residue for its enzymatic activity (7). These factors limit the feasibility of directly targeting GPX4 in clinical applications (8). Understanding the mechanisms underlying the regulation of GPX4 protein in cancer cells and identifying exploitable approaches to target GPX4 regulation will facilitate the development of ferroptosis-based treatment for cancer.

Liver cancer is a leading cause of cancer-related mortality worldwide, but treating advanced-stage liver cancer is challenging due to limited therapeutic options (9–11). Current standard treatments, including receptor tyrosine kinase (RTK) inhibitors such as sorafenib and lenvatinib (12, 13) and immunotherapy combinations like atezolizumab with bevacizumab, offer only modest improvements in overall survival (14, 15). Recent preclinical studies have proposed ferroptosis induction as a promising strategy to combat established liver cancer. For instance, inhibition of apurinic/apyrimidinic endonuclease 1 (APE1) enhances ferroptosis through regulation of the NRF2/SLC7A11/GPX4 axis (16). Moreover, concurrent induction of ferroptosis and myeloid-derived suppressor cells (MDSCs) blockade has demonstrated potential in sensitizing liver tumors to immune checkpoint inhibition (17). The phosphorylation of GPX4 at S104, mediated by creatine kinase B (CKB), has been shown to inhibit the degradation of GPX4, which can be targeted for the treatment of liver cancer (18). Due to the challenges of directly targeting GPX4, developing effective methods to induce ferroptosis, guided by a comprehensive understanding of GPX4 regulation, may represent a promising therapeutic innovation for liver cancer treatment.

To address these issues, we conducted FACS-based genome-wide CRISPR screening in liver cancer cells, identifying mucosa-associated lymphoid tissue lymphoma

## Significance

GPX4, an antioxidant defense enzyme, is a critical regulator of ferroptosis by neutralizing lipid hydroperoxides. However, our understanding of the mechanisms underlying the regulation of GPX4 remains limited. In this study, we provide unique mechanistic insights into GPX4 regulation, showing that MALT1 stabilizes GPX4 by protecting it from ubiquitin-mediated degradation through the specific cleavage of the E3 ubiquitin ligase RC3H1. The MALT1–RC3H1 axis represents a promising therapeutic target for inducing ferroptosis in liver cancer cells. Pharmacological inhibition of MALT1 with MI-2 induces ferroptosis and shows strong synergistic effects when combined with sorafenib or regorafenib across various cancer types, including liver, thyroid, kidney, and colorectal cancers, highlighting the translational potential of our findings for the development of novel therapeutic strategies.

Reviewers: S.H., McGill University; and E.P., Hebrew University-Hadassah Medical School.

The authors declare no competing interest.

Copyright © 2024 the Author(s). Published by PNAS. This article is distributed under Creative Commons Attribution-NonCommercial-NoDerivatives License 4.0 (CC BY-NC-ND).

<sup>1</sup>J.W., L.L., B.M., and B.Y. contributed equally to this work.

<sup>2</sup>To whom correspondence may be addressed. Email: wxqin@sjtu.edu.cn, c.sun@dkfz.de, r.bernards@nki.nl, or cwang@shsci.org.

This article contains supporting information online at <https://www.pnas.org/lookup/suppl/doi:10.1073/pnas.2419625121/-DCSupplemental>.

Published December 31, 2024.

translocation protein 1 (MALT1) as a key molecular regulator of GPX4. We further investigated the mechanisms by which MALT1 regulates GPX4 stability and explored the potential of targeting MALT1 to induce ferroptosis in liver cancer cells. Ultimately, we delineated a therapeutic strategy that synergistically induces ferroptosis by targeting MALT1 in combination with sorafenib or regorafenib across various cancer types.

## Results

**Identification of MALT1 as a Modulator of GPX4 Protein.** To evaluate the potential of leveraging ferroptosis as a therapeutic approach in liver cancer, we first examined the expression levels of GPX4 in HCC tissues. We observed significant upregulation of GPX4 mRNA in tumor tissues compared to adjacent nontumor tissues (*SI Appendix*, Fig. S1*A*). Furthermore, in a cohort of 365 HCC patients, those with the highest levels of GPX4 mRNA in their tumors experienced the poorest survival outcomes (Fig. 1*A*). Importantly, genetic inhibition of GPX4 markedly suppressed the proliferation of Huh7 and SK-Hep1 cells (*SI Appendix*, Fig. S1 *B–D*). Collectively, these findings suggest that GPX4 could serve as a potential therapeutic target for liver cancer treatment.

To systematically elucidate the molecular regulators of GPX4, we conducted a genome-wide fluorescence-activated cell sorting (FACS)-based CRISPR screening to identify potential candidates that modulate GPX4 expression (Fig. 1*B*). PLC/PRF/5 cells were selected for the FACS-based CRISPR screening because PLC/PRF/5 cells are relatively resistant to GPX4 knockdown (*SI Appendix*, Fig. S1 *E–G*), whereas knockdown of GPX4 significantly suppressed the proliferation of Huh7 and SK-Hep1 cells, which are therefore not suitable for screening assay. Through bioinformatics analysis, we identified 40 positive and 113 negative regulators of GPX4 protein levels (Fig. 1*C* and **Dataset S1**). As expected, GPX4 gRNAs were enriched in the GPX4<sup>low</sup> cell population, underscoring the reliability of the genetic screening (**Dataset S1**). Notably, EEFSEC (eukaryotic elongation factor, selenocysteine-tRNA specific) and FBXW7 (F-box and WD repeat domain containing 7) were identified as regulators of GPX4 expression, consistent with their known involvement in ferroptosis regulation (Fig. 1*D*) (19–21). Interestingly, the gene encoding MALT1 emerged as one of the most significant hits (Fig. 1*D*). MALT1 acts as a distinctive paracaspase that cleaves substrates after arginine or lysine residues, leading to protein degradation (22). However, the role of MALT1 in ferroptosis and how MALT1 regulates GPX4 expression remain unknown.

To validate the screening findings, we generated MALT1-knockout PLC/PRF/5 and Hep3B cells and assessed GPX4 protein levels. In PLC/PRF/5, MALT1-knockout cells exhibited comparable mRNA levels but significantly reduced GPX4 protein levels compared to control cells (Fig. 1 *E* and *F*). In Hep3B cells, while a 40 to 50% reduction in GPX4 mRNA levels was observed in MALT1-knockout cells, this did not fully correspond to the nearly complete loss of GPX4 protein. These results suggest that the regulation of GPX4 occurs, at least in part, at the posttranscriptional level (Fig. 1 *E* and *F*). Supporting this hypothesis, we found that the reduction in GPX4 protein levels caused by MALT1-knockout could be mitigated by the proteasome inhibitor MG132 and enhanced by the protein synthesis inhibitor, cycloheximide (CHX) (Fig. 1*G* and *SI Appendix*, Fig. S2*A*). Additionally, we observed elevated levels of GPX4 ubiquitination in MALT1-knockout cells (Fig. 1*H*), suggesting that MALT1 plays a crucial role in regulating GPX4 stability. Subsequently, we

confirmed that MALT1-knockout increased the susceptibility of liver cancer cells to ferroptosis induced by GPX4 inhibitors RSL3 or ML210 (Fig. 1 *I* and *J*).

Through bioinformatics analysis, we identified a positive correlation between MALT1 and GPX4 protein levels across CCLE pan-cancer cell lines, with particularly strong correlations observed in liver cancer cell lines. This finding was further supported in our cell line panel (*SI Appendix*, Fig. S2 *B* and *C* and Fig. 1*K*). However, no substantial correlation was detected at the mRNA level for these two genes (*SI Appendix*, Fig. S2*D*). Tissue array analysis of MALT1 and GPX4 in 75 human HCC tissues revealed a significant positive correlation between their protein levels (Fig. 1 *L* and *M*), lending additional support to the positive regulatory relationship between MALT1 and GPX4.

### MALT1 Stabilizes GPX4 through Cleavage of E3 Ubiquitin Ligase RC3H1.

To investigate the mechanisms by which MALT1 regulates GPX4 ubiquitination, we performed a proteomic analysis on control and MALT1-knockout PLC/PRF/5 cells, identifying 1,427 differentially expressed proteins. We then overlapped these differentially expressed proteins with our FACS screening data, revealing 16 proteins that modulate GPX4 protein levels (Fig. 2 *A* and *B* and **Datasets S1** and **S2**). Among these, RC3H1 was further identified from the Human E3 Ubiquitin Ligase database, based on the MALT1's regulatory role on GPX4 ubiquitination (Fig. 2*C* and **Datasets S1** and **S2**). RC3H1 has previously been reported to be a proteolytic substrate of MALT1 (23–25). Indeed, MALT1 ablation increased RC3H1 protein expression while reducing its cleavage compared to control cells (Fig. 2 *D* and *E*).

After establishing a connection between the MALT1–RC3H1 axis and GPX4 protein regulation, we further investigated the underlying mechanism by which RC3H1 modulates GPX4 protein level. We first proceeded with coimmunoprecipitation analyses to investigate potential interactions between GPX4 and RC3H1. Our findings revealed a notable interaction between these two proteins (Fig. 2*F*). Furthermore, we observed that knockdown of RC3H1 in liver cancer cells led to a substantial increase in GPX4 protein levels, accompanied by reduced GPX4 ubiquitination (Fig. 2 *G–I*). Conversely, overexpression of RC3H1 enhanced the ubiquitin-dependent degradation of GPX4 protein (Fig. 2 *J* and *K*) and knockdown of RC3H1 could block the reduction in GPX4 protein levels facilitated by cycloheximide (CHX) (Fig. 2*L*). More importantly, interference with RC3H1 in MALT1-deficient cells reversed ubiquitin-dependent degradation of GPX4 expression (Fig. 2*M*). Collectively, these data suggest that MALT1 inhibits GPX4 degradation through cleavage of E3 ubiquitin ligase RC3H1.

**MALT1 Inhibition Triggers Ferroptosis in Liver Cancer Cells.** The crucial regulatory role of the MALT1–RC3H1 axis on GPX4 protein prompted us to investigate the potential of targeting MALT1 as an approach to induce ferroptosis. We conducted a compound screening involving 2,103 compounds on two ferroptosis-sensitive liver cancer cell lines, focusing on identifying potential ferroptosis inducers evidenced by the rescue effects of ferrostatin-1 on cell viability (Fig. 3*A*, *SI Appendix*, Fig. S3*A*, and **Dataset S3**). The compound screening assay identified MI-2, EX 527 (selisistat), and AI-10-49 as potential candidate drugs capable of inducing ferroptosis in both cell lines (Fig. 3 *B* and *C*). EX 527 (selisistat) and AI-10-49 were excluded from further analysis due to high-concentration requirements and narrow concentration range of rescue effects, respectively (*SI Appendix*, Fig. S3 *B* and *C*). MI-2, originally identified as an inhibitor of MALT1 protease, has shown notable efficacy against activated B cell-like diffuse large B

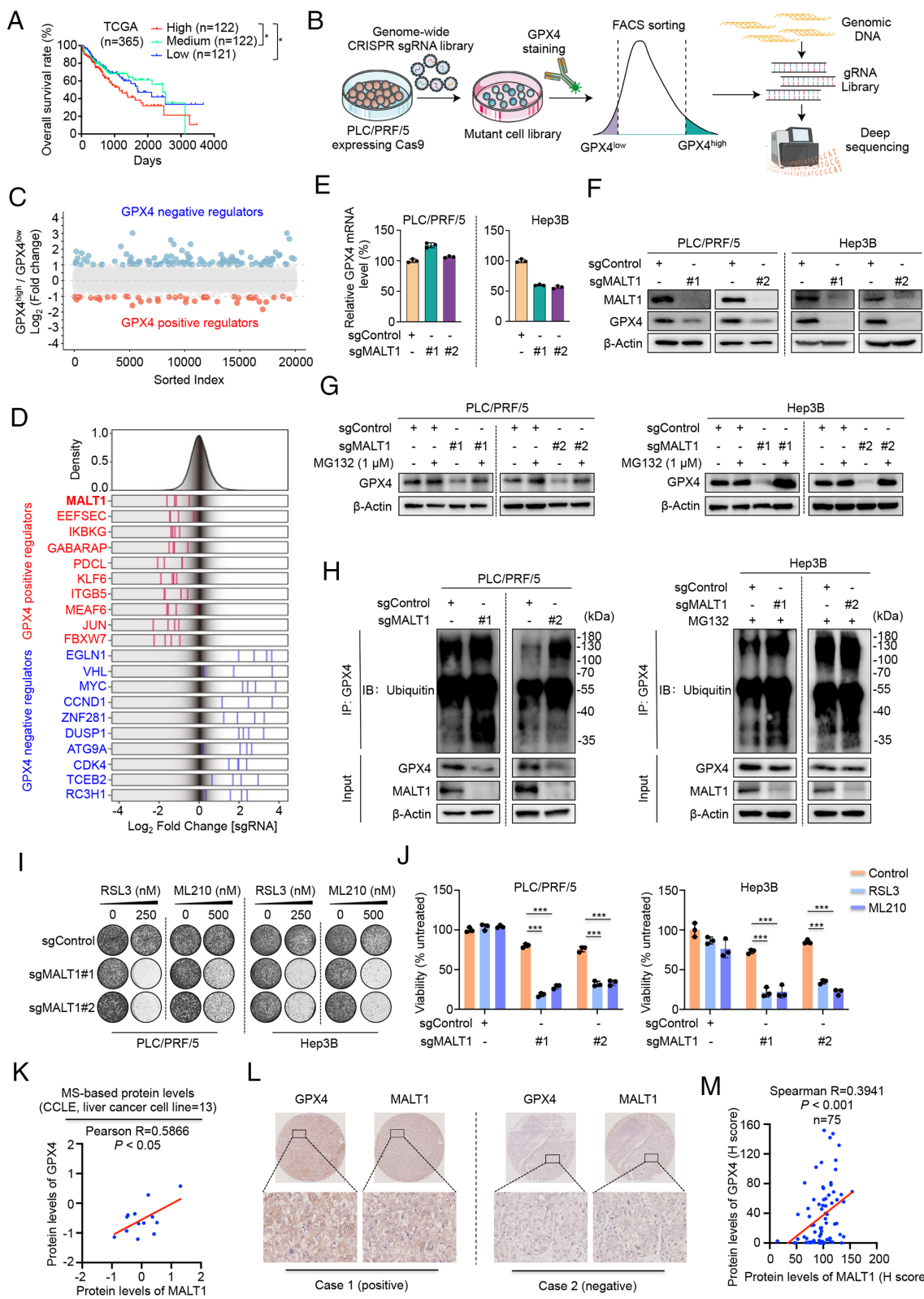


**Fig. 1.** Identification of MALT1 as a modulator of GPX4 expression. (A) Kaplan-Meier survival curves indicating that high levels of GPX4 mRNA correlate with poor prognosis in patients with HCC from the TCGA cohort ( $n = 365$ ). \* $P < 0.05$ . (B) Schematic overview of the flow cytometry-based pooled CRISPR screening to identify modulators of GPX4 expression. Blue indicates negative regulators, while red indicates positive regulators of GPX4. (E and F) GPX4 mRNA and protein levels in MALT1-knockout and control PLC/PRF/5 and Hep3B cells, measured by qRT-PCR (mean  $\pm$  SD,  $n = 3$ ) (E) and western blot (F), respectively. (G) Western blot analysis of GPX4 protein levels in MALT1-knockout and control PLC/PRF/5 and Hep3B cells treated with or without MG132 (1  $\mu$ M), a proteasome inhibitor. (H) Endogenous GPX4 ubiquitination levels in MALT1-knockout and control PLC/PRF/5 and Hep3B cells, detected by western blots. (I) Colony formation assays in MALT1-knockout and control PLC/PRF/5 and Hep3B cells, treated with RSL3 or ML210 at indicated concentrations for 10 to 14 d. (J) Quantification of CellTiter-Blue viability assays of MALT1-knockout and control PLC/PRF/5 and Hep3B cells exposed to RSL3 or ML210 (mean  $\pm$  SD,  $n = 3$ ). \*\*\* $P < 0.001$ . (K) Correlation analysis of MALT1 and GPX4 protein expression in 13 liver cancer cell lines (excluding JHH1) from the CCLE dataset. (L) Representative immunohistochemical staining of GPX4 and MALT1 in liver cancer tissues. (M) Correlation analysis between MALT1 and GPX4 protein expression in liver cancer tissues ( $n = 75$ ).

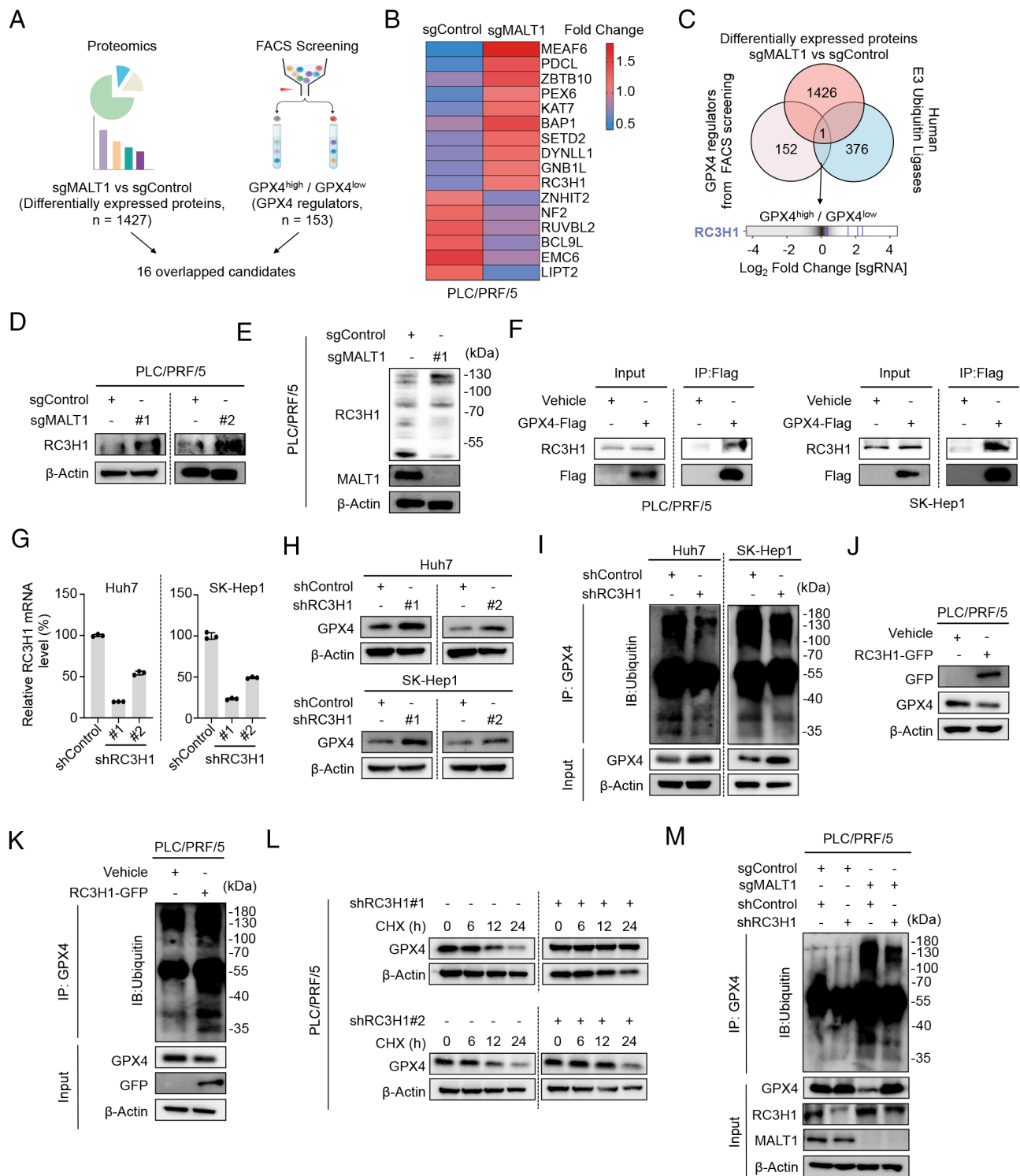


**Fig. 2.** MALT1 regulates GPX4 stability by cleaving the E3 ubiquitin ligase RC3H1. (A) Strategy used to identify candidate proteins mediating MALT1's regulatory role on GPX4 protein stability. (B) Heatmap displaying differentially expressed candidate proteins with modulatory effects on GPX4 level between MALT1-knockout and control PLC/PRF/5 cells from quantitative proteomics data. (C) RC3H1 was the only E3 ubiquitin ligase differentially expressed between MALT1-knockout and control PLC/PRF/5 cells, while also identified as a modulator of GPX4 expression in FACS-based genome-wide screening. (D) RC3H1 protein levels in control and MALT1-knockout PLC/PRF/5 cells measured by western blot. (E) Cleavage reaction determined by western blot analysis of RC3H1 in MALT1-knockout PLC/PRF/5 cells. (F) Immunoprecipitation (IP) of Flag-tagged GPX4 from PLC/PRF/5 and SK-Hep1 cells, followed by western blot analysis of RC3H1 and Flag. (G) qRT-PCR analysis of RC3H1 mRNA levels in RC3H1-knockdown Huh7 and SK-Hep1 cells (mean ± SD, n = 3). (H) Western blot analysis of GPX4 protein levels in RC3H1-knockdown Huh7 and SK-Hep1 cells using western blot. (I) Detection of endogenous GPX4 ubiquitination levels in RC3H1-knockdown Huh7 and SK-Hep1 cells using western blot. (J) GPX4 expression levels assessed by western blot in PLC/PRF/5 cells transfected with GFP-tagged RC3H1 expression plasmids. (K) GPX4 ubiquitination levels detected in RC3H1-overexpressing PLC/PRF/5 cells. (L) Western blot analysis of GPX4 protein levels in RC3H1-knockdown PLC/PRF/5 cells treated with cycloheximide (CHX, 50 µg/mL), a protein synthesis inhibitor. (M) Endogenous GPX4 ubiquitination levels assessed in control and MALT1-knockout PLC/PRF/5 cells with or without RC3H1 additional knockdown, demonstrated by western blot analysis.

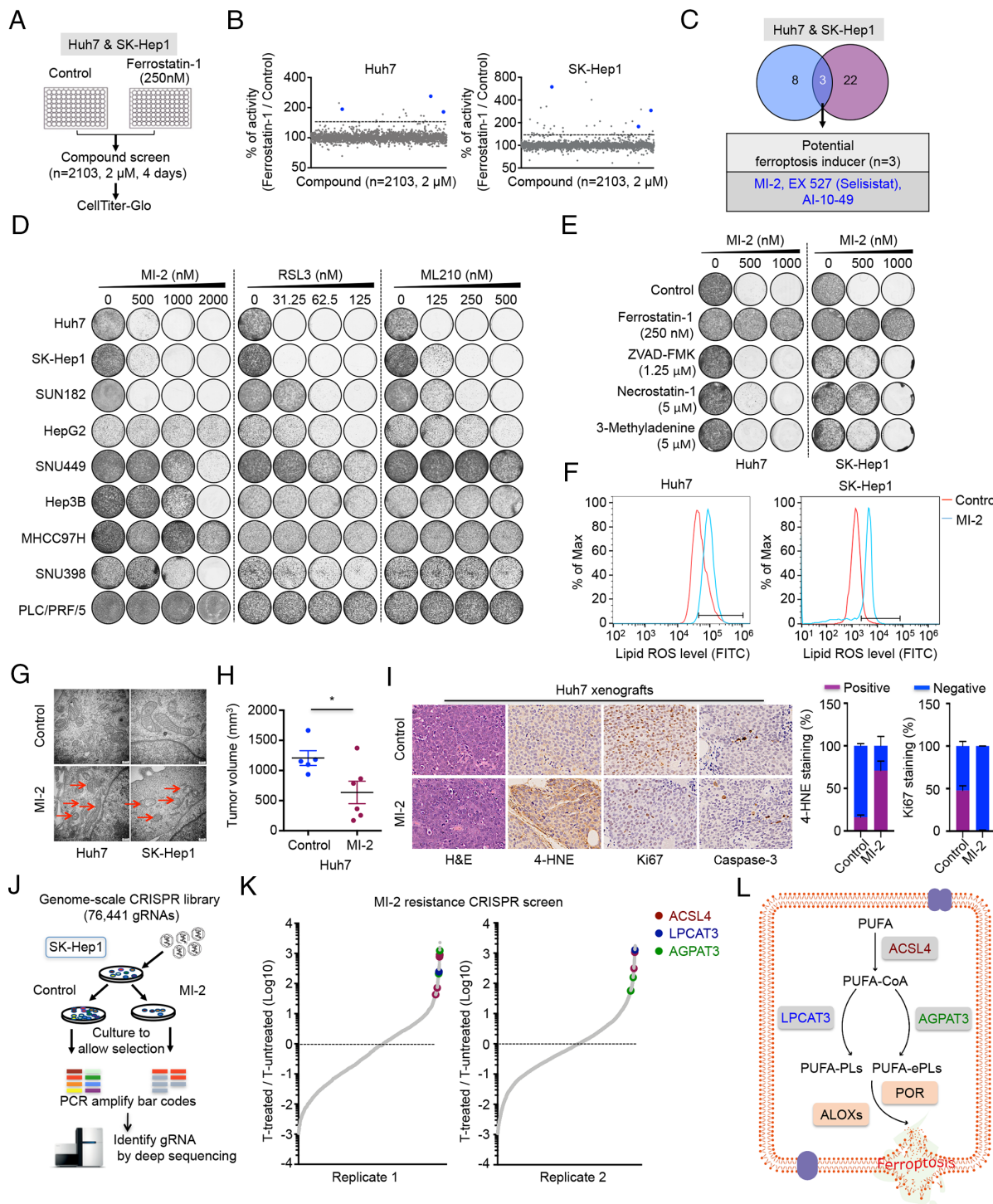


**Fig. 3.** Targeting MALT1 induces ferroptosis in liver cancer cells. (A) Schematic outline of the compound screening. Huh7 and SK-Hep1 cells were treated with a compound library containing FDA-approved drugs and bioactive targeted compounds (n = 2,103, 2  $\mu$ M) in the presence or absence of the ferroptosis inhibitor ferrostatin-1 (250 nM) for 4 d in duplicate. Cell viability was assessed by CellTiter-Glo. (B and C) Three compounds (MI-2, EX 527, AI-10-49) identified as potential ferroptosis inducers in both Huh7 and SK-Hep1 cells, as evidenced by the rescue effects of ferrostatin-1 on cell viability (at least 1.5-fold increase in the group treated with a combination of the compound and ferrostatin-1 compared to the group treated with the compound alone). (D) Colony formation assays performed on liver cancer cell lines treated with increasing concentrations of MI-2, RSL3, or ML210, respectively. (E) Colony formation assays performed on indicated cell lines treated with MI-2 combined with ferrostatin-1, ZVAD-FMK, necrostatin-1, or 3-Methyladenine, respectively for 10 to 14 d. Ferrostatin-1, the ferroptosis inhibitor; ZVAD-FMK, the apoptosis inhibitor; necrostatin-1, the necroptosis inhibitor; 3-Methyladenine, the autophagy inhibitor. (F) Huh7 and SK-Hep1 cells were treated with MI-2 (2  $\mu$ M) and C11-BODIPY (2  $\mu$ M) oxidation was assessed by flow cytometry. (G) Ultrastructural analysis of MI-2-treated cells (Huh7 and SK-Hep1) using transmission electron microscopy. Red arrows indicate damaged mitochondria. (H) Tumor volumes of Huh7 tumor xenografts in BALB/c nude mice measured following vehicle or MI-2 (20 mg/kg) treatment for 12 d (mean  $\pm$  SEM, n = 6). \*P < 0.05. (I) Representative images of H&E, 4-HNE, Ki-67, and cleaved caspase-3 staining in Huh7 xenografts of mice treated with either vehicle or MI-2. Quantification of 4-HNE and Ki-67 staining from each group (Right panels). (J) Schematic representation of the genome-wide CRISPR-Cas9 screening performed in SK-Hep1 cells. SK-Hep1 cells were infected with a lentiviral genome gRNA library and cultured for 45 d in the absence (untreated group) or presence of MI-2 (700 nM, treated group) in duplicate. gRNA barcodes of untreated or treated samples were recovered by PCR and analyzed by next-generation sequencing. (K) Depicting the relative abundance of the gRNA barcode sequences from the genome-wide resistance screens. ACSL4, LPCAT3, and AGPAT3 were identified as the candidates whose knockouts conferred resistance to MI-2 treatment. (L) Schematic of the PLOOH biosynthesis pathway. Genes identified from the CRISPR screen are marked in the indicated colors to highlight their contribution to ferroptosis.

cell lymphoma (ABC-DLBCL) in both in vitro and in vivo studies (26). Consistent with our findings, a recent study also discovered that MI-2 induces ferroptosis in vascular smooth muscle cells (27). The identification of MALT1 inhibitor MI-2 as a ferroptosis inducer in such an unbiased compound screening further emphasizes the important role of MALT1 in GPX4 regulation.

Then, we treated a panel of cell lines with increasing concentrations of MI-2 or traditional GPX4 inhibitor (RSL3 or ML210) for 10 to 14 d in colony formation assays. While the response to these compounds varied across cell lines, the effects of MI-2 and GPX4 inhibitors on the panel of liver cancer cell lines were remarkably similar (Fig. 3*D*). Generally, elevated levels of either GPX4 or MALT1 protein expression correlate with reduced sensitivity to MI-2 or GPX4 inhibitors (*SI Appendix*, Fig. S2*C*). It is possible that a high dose of MI-2 or GPX4 inhibitors is required to suppress the expression or activity of GPX4 in cells with higher MALT1/GPX4 expression, which require further investigation. Cell death induced by MI-2 in Huh7, SK-Hep1, and SNU398 cells could be rescued effectively by ferrostatin-1. However, other types of cell death inhibitors were ineffective in suppressing the cell death induced by MI-2 (Fig. 3*E* and *SI Appendix*, Fig. S3*D*). We also observed an increase in lipid reactive oxygen species (ROS) levels and mitochondrial damage in Huh7, SK-Hep1, and SNU398 cells treated with MI-2 (Fig. 3*F* and *G* and *SI Appendix*, Fig. S3 *E* and *F*). Additionally, MI-2 significantly suppressed growth of Huh7 xenografts (Fig. 3*H*), accompanied by increased lipid peroxidation levels evidenced by 4-HNE staining, and decreased proliferation, as indicated by Ki67 staining (Fig. 3*I*).

To further uncover the regulatory network responsible for the sensitivity of MALT1 inhibitor, we conducted an unbiased genome-wide CRISPR screening (Fig. 3*J*). This analysis identified the essential role of three genes (ACSL4, LPCAT3, and AGPAT3) in MI-2-induced cell death (Fig. 3*K* and *Dataset S4*), which are also commonly recognized in ferroptosis induction (Fig. 3*L*).

It is known that therapy-resistant cancer cells often exhibit altered metabolic states that make them susceptible to ferroptosis induction (5, 28). To investigate whether MI-2 maintains the characteristic effects of conventional GPX4 inhibitors on drug-resistant cell lines, we established lenvatinib-resistant and FGFR4 inhibitor BLU554-resistant Hep3B cells (*SI Appendix*, Fig. S3*G*) and treated them with RSL3 or MI-2 in colony formation assays. Interestingly, we found that the resistant cells displayed similar increased sensitivity to both MI-2 and RSL3 treatments, which could be rescued by the addition of ferrostatin-1 (*SI Appendix*, Fig. S3 *H* and *I*).

Collectively, our findings suggest that MI-2 could represent a ferroptosis inducer with potential applications in the treatment of liver cancer.

**MALT1 Inhibitor Down-Regulates GPX4 through Ubiquitination-Mediated Degradation via RC3H1.** Quantitative proteomics analysis revealed that treatment with the MALT1 inhibitor MI-2 led to a reduction of GPX4 protein levels in liver cancer cells, which was confirmed through both in vitro and in vivo validation (Fig. 4 *A–D*). To extend our investigation, we used another MALT1 inhibitor safimaltib and observed similar effects in down-regulating GPX4 protein level without affecting its mRNA level (*SI Appendix*, Fig. S4 *A* and *B*). Since we have found that MALT1-knockout exerts a modulatory effect on GPX4 stability at the posttranscriptional level, we investigated whether MALT1 inhibition would produce similar results. As expected, the reduction in GPX4 protein levels induced by MI-2 could be blocked by the proteasome inhibitor MG132 and facilitated by the protein synthesis inhibitor cycloheximide (Fig. 4 *E* and *F*). Similar effects were not observed when cells were treated

with RSL3 or ML210 (*SI Appendix*, Fig. S4 *C–F*), suggesting a distinct role of the MALT1 inhibitor compared to classic GPX4 inhibitor. Additionally, consistent with MALT1 knockout, MI-2-treated cells exhibited increased ubiquitination of GPX4 (Fig. 4*G*). Considering that MALT1 regulates GPX4 stability by cleaving the E3 ubiquitin ligase RC3H1, we examined the levels of RC3H1 following MI-2 treatment. Compared to control cells, MI-2-treated cells displayed comparable mRNA levels but increased protein expression of RC3H1 (Fig. 4 *H* and *I*). Importantly, RC3H1 knockdown effectively prevented MALT1 inhibition-induced GPX4 downregulation and ubiquitination (Fig. 4 *J* and *K*).

In conclusion, we establish MALT1 as a regulator of GPX4 protein levels. MALT1 inhibition using MI-2 promotes RC3H1-mediated, ubiquitin-dependent degradation of GPX4, a mechanism that can be exploited to induce ferroptosis in liver cancer cells.

### MALT1 Inhibition Is Synergistic with Sorafenib or Regorafenib.

Given that many liver cancer cell lines demonstrate insensitivity to MI-2, we aimed to investigate whether combination treatment could enhance the susceptibility of these cells to ferroptosis induction. Initially, we confirmed that MI-2 effectively reduced GPX4 protein levels in Hep3B, SNU449, and MHCC97H cells, irrespective of their sensitivity to ferroptosis induction (Fig. 5*A*). To determine whether conventional therapeutic drugs used in HCC treatment could synergize with MI-2 in these ferroptosis-insensitive cells, we treated Hep3B, SNU449, and MHCC97H cells with MI-2 and sorafenib, regorafenib, lenvatinib, or the indicated combinations. Strong synergies between MI-2 and sorafenib or regorafenib were observed in all three cell lines (Fig. 5*B* and *SI Appendix*, Fig. S5*A*). However, no synergistic effect was observed when cells were treated with MI-2 and lenvatinib (*SI Appendix*, Fig. S5*A*). Sorafenib, regorafenib, and lenvatinib are all clinically approved multikinase inhibitors used in the treatment of advanced HCC. Regorafenib is structurally similar to sorafenib (9, 29, 30), which may explain the similar synergic effects observed when combining either sorafenib or regorafenib with MI-2. Comparable results were obtained when combining RSL3 with sorafenib or regorafenib (*SI Appendix*, Fig. S5*B*). Furthermore, we observed ferroptosis-specific mitochondrial alterations and increasing lipid peroxides accumulation in liver cancer cell lines treated with sorafenib when combined with MI-2 (Fig. 5 *C* and *D*) or RSL3 (*SI Appendix*, Fig. S5 *C* and *D*).

Given that sorafenib is a multikinase inhibitor, we conducted kinome-based CRISPR screenings to investigate the mechanisms underlying the synergistic lethality of sorafenib. We found that loss of individual kinase targets of sorafenib did not synergize with GPX4 inhibition. However, it remains possible that the synergy with GPX4 inhibition is due to the simultaneous inhibition of multiple kinase targets of sorafenib (*SI Appendix*, Fig. S5*E* and *Dataset S5*). As a multikinase inhibitor, sorafenib has been shown to induce ferroptosis by targeting SLC7A11 (31–33). To further investigate this, we used <sup>15</sup>N labeled L-cysteine to trace cystine uptake and biosynthesis of GSH. As expected, sorafenib treatment induced a notable reduction in both cystine uptake and biosynthesis of GSH, as evidenced by the decreased utilization of <sup>15</sup>N-labeled L-cysteine (Fig. 5*E*). SLC7A11, as one of the subunits of system  $x_c^-$ , plays a crucial role in cystine uptake (34, 35). We found that expression of SLC7A11 was significantly associated with the sensitivity to GPX4 inhibitor in both liver cancer cell line panel and pan-cancer cell lines (*SI Appendix*, Fig. S5*F*). Together, these findings suggest that sorafenib may synergize with MI-2 through its activity against SLC7A11.

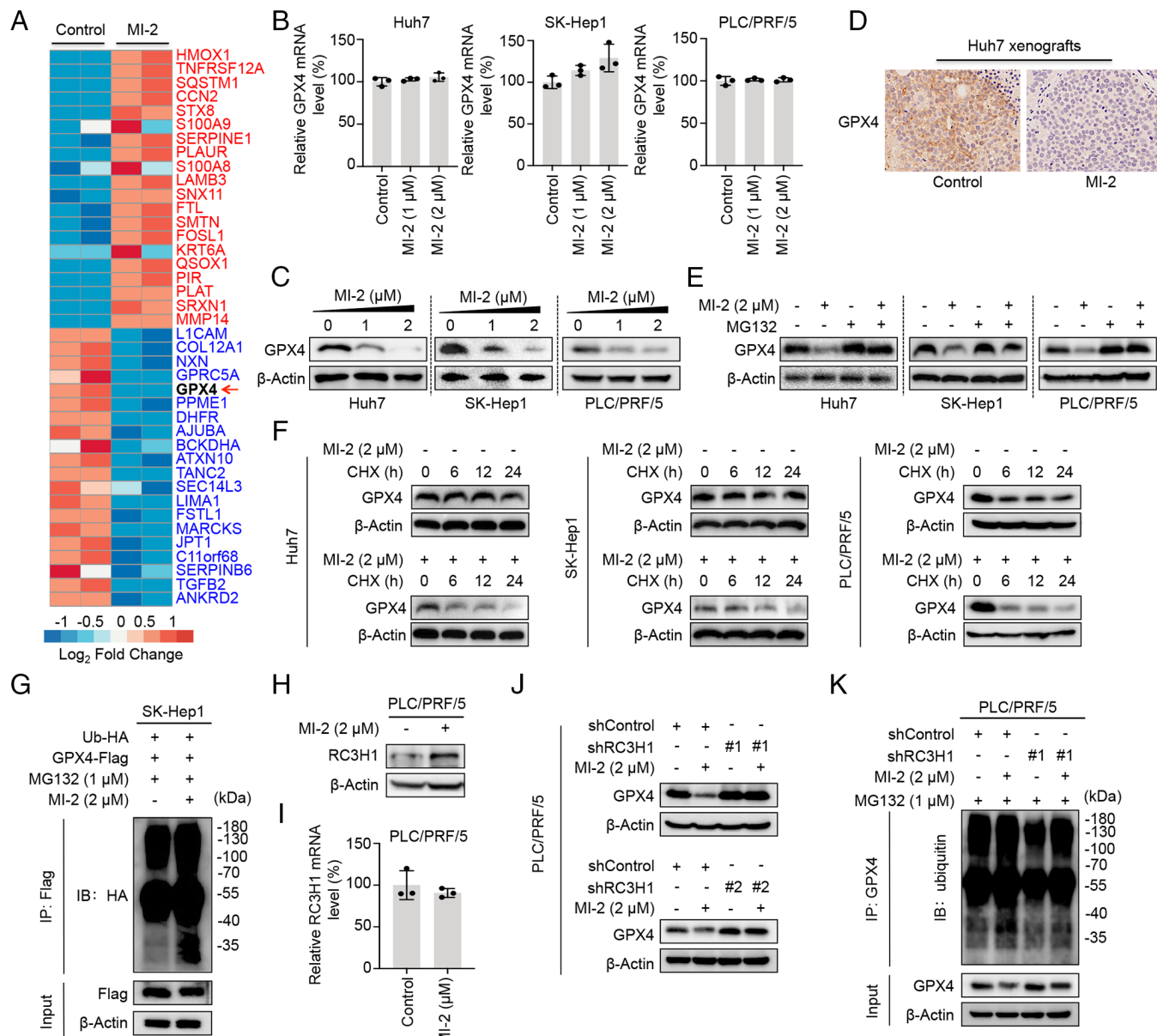


**Fig. 4.** MALT1 inhibition facilitates ubiquitin-dependent degradation of GPX4 protein through RC3H1. (A) Quantitative proteomics analysis of SK-Hep1 cells treated with or without MI-2 (2  $\mu$ M) for 4 d. The red arrow indicates the downregulation of GPX4 upon MI-2 treatment. (B and C) GPX4 mRNA and protein levels in Huh7, SK-Hep1, and PLC/PRF/5 cells treated with MI-2 for 24 to 48 h, assessed by qRT-PCR analyses (mean  $\pm$  SD, n = 3) (B) and western blot (C). (D) Representative images of GPX4 immunostaining in formalin-fixed paraffin-embedded Huh7 xenografts from BALB/c nude mice treated with vehicle or MI-2 (20 mg/kg) for 12 d. (E) Western blot analysis of GPX4 protein levels in Huh7, SK-Hep1, and PLC/PRF/5 cells exposed to MG132 (1  $\mu$ M), MI-2 (2  $\mu$ M), or the combination of both for 24 to 48 h. (F) Western blot analysis of GPX4 protein levels in Huh7, SK-Hep1, and PLC/PRF/5 cells treated with cycloheximide (CHX, 50  $\mu$ g/ml) in the presence or absence of MI-2 (2  $\mu$ M). (G) GPX4 ubiquitination levels in SK-Hep1 cells treated with MI-2, measured by immunoprecipitation followed by western blot analysis. (H and I) RC3H1 protein and mRNA levels in PLC/PRF/5 cells treated with MI-2 (2  $\mu$ M) for 3 d, measured by western blot (H) and qRT-PCR (mean  $\pm$  SD, n = 3) (I), respectively. (J) Western blot analysis of GPX4 protein levels in control or RC3H1-knockdown PLC/PRF/5 cells treated with or without MI-2 (2  $\mu$ M). (K) GPX4 ubiquitination determined by immunoprecipitation and western blot in RC3H1-knockdown PLC/PRF/5 cells treated with or without MI-2 (2  $\mu$ M) in the presence of MG132 (1  $\mu$ M).

In order to enhance the clinical relevance of our findings, we evaluated synergistic effect of this combination in patient-derived liver cancer organoid (PDO) models. The combination of MI-2 and sorafenib notably suppressed the proliferation of these organoids (Fig. 5F). To assess whether these in vitro findings could be recapitulated in vivo, we established subcutaneous tumors in nude mice using MHCC97H cells. Consistent with our in vitro results, the combined administration of MI-2 and sorafenib demonstrated a substantial inhibition of tumor growth, accompanied by decreased GPX4 expression and increased lipid peroxidation levels in tumor tissues (Fig. 5G and H).

Sorafenib has been approved by the FDA for the treatment of thyroid cancer and kidney cancer, while regorafenib, an analog of sorafenib, has been approved for colorectal cancer treatment (12, 13, 36, 37). The remarkable synergy observed between MI-2 and sorafenib in liver cancer cells inspired us to investigate the potential of this combination therapy in treating these three types of cancer. Encouragingly, synergistic effects on cell proliferation were observed when sorafenib or regorafenib was combined with MI-2 in thyroid cancer, kidney cancer, and colorectal cancer cell lines (*SI Appendix*, Fig. S6 A–C). CellTiter-Blue viability assay confirmed that the cell death induced by these combinations was

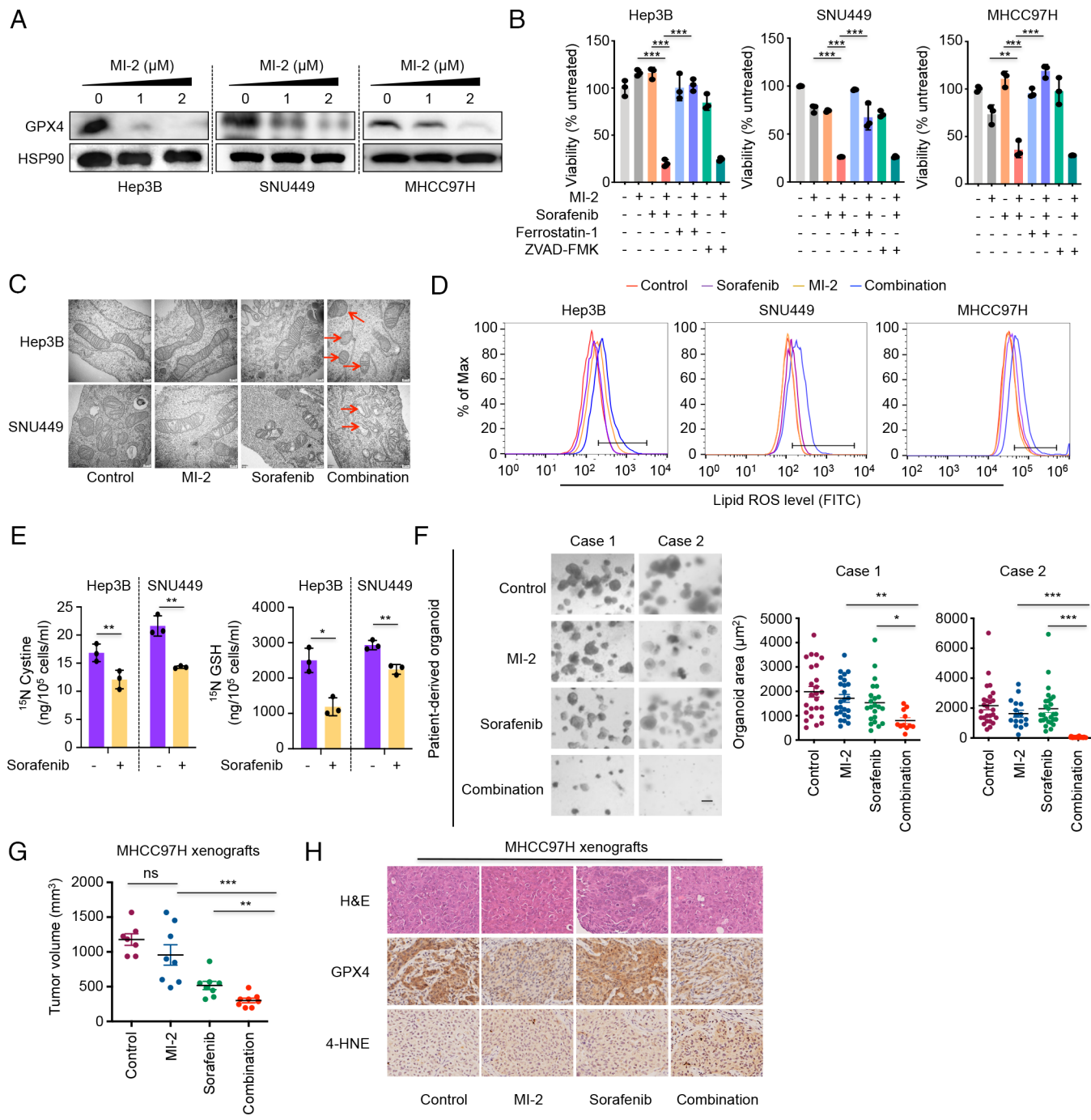


**Fig. 5.** Targeting MALT1 synergies with sorafenib in liver cancer cells. (A) Western blot analysis of GPX4 protein levels in three HCC cell lines (insensitive to ferroptosis induction: Hep3B, SNU449, and MHCC97H) treated with MI-2 for 3 to 4 d. (B) Quantification of CellTiter-Blue viability assays of Hep3B, SNU449, and MHCC97H cells exposed to MI-2 (1 to 2  $\mu\text{M}$ ), sorafenib (2.5  $\mu\text{M}$ ), ferrostatin-1 (250 nM), ZVAD-FMK (1.25  $\mu\text{M}$ ), or the indicated combination (mean  $\pm$  SD,  $n = 3$ ). \*\* $P < 0.01$ , \*\*\* $P < 0.001$ . (C) Ultrastructural analysis of Hep3B and SNU449 cells treated with MI-2, sorafenib, or the combination for 3 d, using transmission electron microscopy. Red arrows indicate damaged mitochondria. (D) Lipid ROS level assessed by C11-BODIPY fluorescence in the Hep3B, SNU449, and MHCC97H cells treated with sorafenib, MI-2, or the combination. (E)  $^{15}\text{N}$  labeled L-cysteine was added to the cell culture medium. Cystine uptake ( $^{15}\text{N}$  cystine and  $^{15}\text{N}$  GSH level) was assessed in Hep3B and SNU449 cells upon sorafenib (10  $\mu\text{M}$ ) treatment for 3 d (mean  $\pm$  SD,  $n = 3$ ). \* $P < 0.05$ , \*\* $P < 0.01$ . (F) Representative images showing the response of patient-derived organoids (PDOs) to MI-2 (1  $\mu\text{M}$ ), sorafenib (2.5  $\mu\text{M}$ ), or the combination of both. (Scale bars, 200  $\mu\text{m}$ .) Quantification of organoids (Right panels). \* $P < 0.05$ , \*\* $P < 0.01$ , \*\*\* $P < 0.001$ . (G) Tumor volumes of MHCC97H xenografts in BALB/c nude mice following vehicle, MI-2 (20 mg/kg), sorafenib (30 mg/kg), or combination treatment for 14 d (mean  $\pm$  SEM,  $n = 8$ ). \*\* $P < 0.01$ , \*\*\* $P < 0.001$ . (H) Representative images of H&E, GPX4, and 4-HNE staining performed on formalin-fixed paraffin-embedded MHCC97H xenografts.

attributable to ferroptosis, as evidenced by the rescue effects of ferrostatin-1 (SI Appendix, Fig. S6 H and J). Furthermore, an increase in lipid ROS levels was noted in KTC-1, OSRC-2, and LoVo cells upon combination treatment (SI Appendix, Fig. S6 G). Consistent with in vitro results, mice bearing OSRC-2 and LoVo xenografts that received combination therapy exhibited a significant reduction in tumor burden compared to those receiving monotherapy

(SI Appendix, Fig. S6 H and J). Ferroptosis induction in vivo was also evident in tumor tissues with combination treatment, as demonstrated by GPX4 and 4-HNE staining (SI Appendix, Fig. S6 I and K). Collectively, these findings suggest that combining sorafenib or regorafenib with GPX4 inhibition using MI-2 could represent a broadly applicable strategy for a diverse range of malignancies.

## Discussion

Targeting GPX4 to promote ferroptosis has emerged as a promising cancer treatment strategy; however, the development of effective GPX4 inhibitors has proven to be challenging. Recent research has revealed that GPX4 is regulated through various mechanisms, including transcriptional control and posttranslational modifications (PTMs), suggesting that targeting these regulatory processes could provide an alternative approach for inducing ferroptosis. Studies have uncovered specific mechanisms involved in the regulation of GPX4. For instance, ZEB1, a transcription factor, inhibits GPX4 transcription in cancer cells by binding to the E-box motifs (38), while OTUD5 confers ferroptosis resistance by stabilizing GPX4 (39, 40). Despite these findings, our understanding of the mechanisms governing GPX4 regulation remains limited, and current knowledge is still insufficient for identifying effective strategies for ferroptosis induction. In a recent study, through In-Cell Western assays along with a drug screening, Li et al. identified the compound N6F11 promotes the degradation of GPX4 by triggering TRIM25-mediated K48-linked ubiquitination of GPX4 in cancer cells (41). From a different perspective, we conducted a FACS-based genome-wide genetic screen to systematically identify modulators of GPX4. Unexpectedly, we found that MALT1, previously recognized as a potential therapeutic target in ABC-DLBCL, emerged as one of the most significant regulators of GPX4 levels. Genetic knockout or pharmacological inhibition of MALT1 using MI-2 effectively induces the ubiquitination of GPX4 and facilitates specific ferroptosis in cancer cells, which have been validated not only through functional experiments but also via unbiased compound screening and functional genetic screening. These findings underscore the specific effects of MI-2 in targeting GPX4 regulation and hold significant promise as a foundational step toward the development of drug-like inhibitors for GPX4 regulation. Concerns have been raised regarding the long-term safety of MALT1 inhibition, as congenital disruption of the MALT1 protease in mice is associated with a rapid, dose-dependent reduction in regulatory T cells, leading to the progressive development of immune abnormalities (42). Despite these challenges, some studies have also shown that an uncoupling of anti-inflammatory effects of MALT1 inhibition from reduction of regulatory T cells can be achieved (43). Therefore, the balance between the safety risks and antitumor effects of MALT1 inhibitors warrants further investigation.

Recent research has elucidated the dual roles of MALT1 as both a protease and a scaffold protein (44, 45). Our study reveals a critical role of MALT1 in regulating GPX4 expression by maintaining its stability through a proteasome-dependent mechanism. We demonstrated that MALT1 deficiency or inhibition by MI-2 leads to increased GPX4 ubiquitination and decreased GPX4 expression levels, resulting in heightened cellular sensitivity to ferroptosis. Although MALT1 is not an E3 ubiquitin ligase, it may modulate the activity of other components within the ubiquitin machinery, highlighting its multifaceted role in cellular processes beyond its established function in immune signaling. By combining proteomic analysis with FACS-based genetic screening, we identified RC3H1, a RING finger E3 ubiquitin ligase, as a key regulator mediating MALT1's involvement in the ubiquitination and proteasomal degradation of GPX4 protein. MALT1 stabilizes GPX4 through the specific cleavage of RC3H1, which directly binds to GPX4 and facilitates its ubiquitination and subsequent proteasomal degradation. Our identification of the MALT1–RC3H1 axis regulating GPX4 adds a layer of complexity to the posttranslational regulation of GPX4. Future research should prioritize the detailed mapping of the interacting domains between

RC3H1 and GPX4, as well as the identification of the specific lysine residues on GPX4 that are ubiquitinated by RC3H1. Such insights will further enhance our understanding of the molecular dynamics governing GPX4 regulation.

Combining different agents with ferroptosis inducers has shown promise in enhancing the susceptibility of cancer cells to ferroptosis induction (46–48). In our study, we utilized sorafenib or regorafenib as combination agents to induce ferroptosis. Both sorafenib and regorafenib exhibited synergistic effects when combined with MALT1 inhibitor or RSL3 in inducing ferroptosis. Additionally, both our findings and other studies have indicated that sorafenib exerts activity against SLC7A11, a key component involved in ferroptosis regulation (49). This synergy can be attributed to the cotargeting of SLC7A11 and GPX4, key components of system  $\text{x}_c^-$ -GSH–GPX4 axis, which helps overcome the intrinsic resistance of cancer cells to ferroptosis induction. Considering that sorafenib or regorafenib has been approved for use in various cancer types, including advanced liver cancer, thyroid cancer, kidney cancer, and colorectal cancer, this combination strategy holds potential for further investigation.

In our study, through FACS-based genome-wide CRISPR screening, we identified the MALT1–RC3H1 axis as a critical regulator of GPX4 protein stability. MALT1 stabilizes GPX4 from ubiquitin-mediated degradation by specifically cleaving the E3 ubiquitin ligase RC3H1. The MALT1 inhibitor MI-2 demonstrates the capacity to induce ferroptosis, which is synergistic with sorafenib and regorafenib across various cancer types.

## Materials and Methods

Our research complies with all relevant ethical regulations. The collection and use of clinical materials were approved by the Eastern Hepatobiliary Hospital Research Ethics Committee. All animal protocols were approved by the Animal Research Ethics Committee of Shanghai Jiao Tong University and were performed following the guidelines for the use of laboratory animals.

**Human Cell Lines and Culture Conditions.** The human cell lines, Hep3B (HB-8604), SK-Hep1 (HTB-52), PLC/PRF/5 (CRL-8024), HepG2 (CRL-11997), SNU398 (CRL-2233), SNU182 were obtained from ATCC. Huh7 (RCB1366) cell line was sourced from RIKEN (Tokyo, Japan). The MHCC97H cell line was provided by the Liver Cancer Institute of Zhongshan Hospital (Shanghai, China). CAL-62 (CL-0618) was obtained from Procell (Wuhan, China). These cell lines were cultured in a controlled environment at 37 °C with 5% CO<sub>2</sub> in Dulbecco's Modified Eagle Medium (DMEM) with 10% fetal bovine serum (FBS), 2 mM glutamine, and 1% penicillin/streptomycin. LoVo (CCL-229) cell line was obtained from ATCC and cultured in F-12 K medium with 10% FBS, 1% penicillin/streptomycin, and 2 Å mM glutamine at 37 °C with 5% CO<sub>2</sub>. SW480 (CCL-228) cell line was obtained from ATCC. OS-RC-2 (RCB0735) cell line was sourced from RIKEN (Tokyo, Japan). KTC-1 was obtained from Shanghai Institutes for Biological Sciences (Shanghai, China). These cell lines were cultured at the same controlled conditions mentioned above but in RPMI-based medium supplemented with 10% FBS, 1% penicillin/streptomycin, and 2 mM glutamine. ACHN (CRL-1611) cell line was obtained from ATCC and cultured in MEM with 10% FBS, 1% penicillin/streptomycin, and 2 Å mM glutamine at 37 °C with 5% CO<sub>2</sub>. The presence of mycoplasma was tested by PCR-based assays. The identities of all the cell lines were confirmed using STR profiling.

**Compounds and Antibodies.** MI-2 (Cat# S7429), 1S,3R-RSL3 (Cat# S8155), ferrostatin-1 (Cat# S7243), ZVAD-FMK (Cat# S7023), erastin (Cat# S7242), EX 527 (Cat# S1541), regorafenib (Cat# S1178), lenvatinib (Cat# S1164), sorafenib (Cat# S1040), safimaltib (Cat# S9896), cycloheximide (Cat# S7418), necrostatin-1 (Cat# S8037), and 3-Methyladenine (Cat# S2767) were purchased from Selleck Chemicals. AI-10-49 (Cat# S80232) was purchased from Shanghai Yuanye Bio-Technology. ML210 (Cat# SML0521) and MG132 (Cat# M7449) were purchased from Sigma-Aldrich. Antibodies against GPX4 (Cat# ab125066), Ki67 (Cat# ab16667), and caspase-3 (Cat# ab32351) were purchased from Abcam. Antibodies against β-actin (Cat# HRP-60008), GAPDH (Cat# HRP-60004),

and GPX4 (Cat# 67763-1-Ig, for immunoprecipitation) were purchased from Proteintech. Antibodies against HA-tag (Cat# 3724S) and Flag-tag (Cat# 14793) were purchased from Cell Signaling Technology. Antibody against MALT1 (Cat# sc-46677) was purchased from Santa Cruz Biotechnology. Antibody against RC3H1 (Cat# PSL-7251) was purchased from ProSci Incorporated. Antibody against 4-HNE (Cat# MAB3249) was purchased from R&D Systems.

**FACS-Based CRISPR-Cas9 Screening.** Fluorescence-activated cell sorting (FACS)-based genome-wide CRISPR screens were performed using Brunello lentiviral pooled libraries in PLC/PRF/5 cells. The cells selected by puromycin were first stained with LIVE/DEAD™ Fixable Near-IR Dead Cell Stain (Cat# L10119, Invitrogen) to exclude nonviable cells, and then fixed and permeabilized with Fixation/Permeabilization solution (Cat# 88-8824-00, Thermo Fisher Scientific). After washing, the cells were incubated with the anti-GPX4 antibody for 45 min at 4 °C, followed by incubation with the appropriate dilutions of Alexa Fluor secondary antibody for 30 min at 4 °C in the dark. The cells were then washed with FACS buffer, and the top 5% (cells with the highest signals) and bottom 5% (cells with the lowest signals) populations were sorted and collected for deep sequencing and bioinformatic analysis.

**Established Stable Cells.** All shRNAs targeting GPX4 and RC3H1 in the PLKO vector were obtained from TRC\_2 human shRNA (Lenti) library. For MALT1-knockout cells, two gRNAs targeting MALT1 were cloned into lentiCRISPR v2 for lentivirus production. Lentivirus were produced through transient transfection of HEK293T cells using jetPRIME® Versatile DNA/siRNA transfection reagent (Cat# PT-114-15, Polyplus Transfection). HEK293T cells were cultured in 10-cm tissue culture dishes and then cotransfected with the lentiviral transfer plasmid and packaging vectors (psPAX2 and pMD2.G). The viral supernatant was harvested 48 h after transfection and filtered through a 0.45 μm filter. Huh7, SK-Hep1, PLC/PRF/5, and Hep3B cells were subsequently infected with lentivirus in the presence of polybrene and propagated for further analysis following selection. The sequences of shRNA and gRNA are listed in [Dataset S6](#).

**qRT-PCR.** Total RNA was extracted from cells using FastPure Cell/Tissue Total RNA Isolation Kit V2 (Cat# RC112, Vazyme). Complementary DNA was synthesized from 1 μg of RNA using HisyGo RT Red SuperMix (Cat# RT101, Vazyme). qRT-PCR was performed using ChamQ Blue Universal SYBR qPCR Master Mix (Cat# Q312, Vazyme). Primer sequences are shown in [Dataset S6](#). The relative mRNA levels were normalized to housekeeping genes.

**Western Blotting.** An equal amount of total protein lysates was separated using 8 to 12% SDS-PAGE and then transferred onto PVDF membranes. The membranes were blocked with 5% fat-free dried milk dissolved in Tris-buffered saline with 0.5% Tween-20 (TBST) for 1 to 2 h. The membranes were then incubated overnight at 4 °C with the corresponding primary antibodies. Following that, the membranes were washed with TBST and then incubated in horseradish peroxidase-conjugated (HRP-conjugated) secondary antibodies for 1 h. Then membranes were washed with TBST for three times, followed by ECL detection.

**Proteomic Analysis.** In brief, at least  $2 \times 10^6$  cells were collected and ground with liquid nitrogen into cell powder. Afterward, four volumes of lysis buffer (8 M urea, 1% protease inhibitor cocktail) was added to the cell powder, followed by sonication 3 min on ice using a high-intensity ultrasonic processor (Scientz). The samples were cleared by centrifugation at 12,000 × g for 10 min at 4 °C. Following that, the precipitated proteins were obtained using TCA and washed by precooled acetone for three times and dried for 1 min. The protein sample was then redissolved in 200 mM TEAB and dispersed using ultrasound. Trypsin was added at a 1:50 trypsin-to-protein mass ratio for the first overnight digestion. The sample was reduced with 5 mM dithiothreitol for 30 min at 56 °C and alkylated with 11 mM iodoacetamide for 15 min at room temperature in the dark. After that, the peptides were desalted using a Strata X SPE column and analyzed by LC-MS/MS.

**Ubiquitination Assay.** To assess the ubiquitination levels of endogenous GPX4, we generated several cell lines, including MALT1-knockout PLC/PRF/5, Hep3B, RC3H1-knockdown Huh7, SK-Hep1, PLC/PRF/5, RC3H1-overexpressing PLC/PRF/5, and MALT1-knockout PLC/PRF/5 with or without RC3H1 additional knockdown. After cell lysis, the samples were subjected to immunoprecipitation with anti-GPX4 antibody and protein G-conjugated magnetic beads overnight at constant rotation, followed by immunoblotting analysis with anti-ubiquitin antibody.

A transfection of HA-tagged ubiquitin plasmid was conducted to evaluate the ubiquitination levels of Flag-GPX4 in cells. The transfected cells were treated with or without MI-2 in the presence of MG132. Subsequently, the cells were lysed in cold Pierce IP Lysis buffer (Cat# 87787, Thermo Fisher Scientific) and cleared by centrifugation. An appropriate amount of protein was then incubated with anti-Flag beads overnight at a constant rotation. The beads were washed three times with IP lysis buffer, followed by immunoblotting analysis with anti-HA antibody.

**Coimmunoprecipitation.** Flag-tagged GPX4 plasmid was transfected to detect the potential interactions between GPX4 and RC3H1 in PLC/PRF/5 cells. Following this, the transfected cells were lysed in cold Pierce IP Lysis buffer (Cat# 87787, Thermo Fisher Scientific) and centrifuged at 12,000 × g for 30 min. The protein samples were then incubated with anti-Flag beads at 4 °C overnight under constant rotation. After washing three times with cold IP buffer, the immunocomplexes were collected for immunoblotting with anti-RC3H1 and anti-Flag antibodies.

**Compound Screens.** Huh7 and SK-Hep1 were screened with a compound library ( $n = 2,103$ , 2 μM) in the presence or absence of 250 nM ferrostatin-1 for 4 d in two replicates. Cell viability was assessed by CellTiter-Glo Cell Viability Assay. Compounds exhibiting an impact on cell viability that could be rescued by ferrostatin-1 (at least 1.5-fold increase in the group treated with combination of the compound and ferrostatin-1 compared to the group treated with the compound alone) were selected for further investigation. The compound library contains FDA-approved drugs as well as bioactive targeted compounds.

**Long-Term Cell Proliferation Assay.** Cells were seeded into 6-well plates at a density of 1.5 to  $3 \times 10^4$  cells per well and cultured in medium supplemented with the specified drugs for duration of 10 to 14 d. Cells were fixed with 4% formaldehyde in PBS and subsequently stained with 0.1% crystal violet solution diluted in water.

**Transmission Electron Microscopy.** Cells were fixed in a solution of 2% glutaraldehyde in PBS for 2 h at 4 °C. They were then postfixed in 1% osmium tetroxide for 1 h at 4 °C. Cells were dehydrated in a series of graded ethanol and embedded in epoxy resin. Ultrathin sections were obtained using a LKB V-type ultramicrotome and stained with lead citrate for electron microscopy. Sections were imaged on a HITACHI H-7650 TEM.

**Lipid Peroxidation Assessment.** Briefly, 200,000 to 250,000 cells per well were seeded in 6-well plates and then cells were treated with indicated compounds for 3 to 4 d. Cells were harvested and resuspended in PBS containing C11-BODIPY (581/591) (2 μM) (Cat# D3861, Invitrogen) at 37 °C for 30 min. Subsequently, cells were analyzed using a flow cytometer equipped with a 488 nm laser for excitation. A minimum of 10,000 cells were analyzed per sample.

**Xenografts.** Huh7 cells ( $1 \times 10^7$  cells per mouse) were injected subcutaneously into the right posterior flanks of 6-wk-old BALB/c nude mice (male, 6 mice per group). Tumor volume based on caliper measurements was calculated using a modified ellipsoidal formula: tumor volume = 1/2 length × width<sup>2</sup>. After tumor establishment, the mice were randomly assigned to 6 d per week treatment with vehicle, or MI-2 (20 mg/kg, intraperitoneal injection). For combination treatment assay, MHCC97H, OSRC-2, and LoVo cells ( $1 \times 10^7$  cells per mouse) were injected subcutaneously into the right posterior flanks of 6-wk-old BALB/c nude mice (male, 6 to 8 mice per group). Mice were randomly assigned to different treatment groups: vehicle, MI-2 (20 mg/kg, intraperitoneal injection, 6 d per week), sorafenib (30 mg/kg, oral gavage, 3 or 6 d per week), regorafenib (5 mg/kg, oral gavage, 6 d per week), or a drug combination in which each compound was administered at the same dose and schedule as the single agent.

**CRISPR-Cas9 Genetic Screens.** To identify genes whose knockout may confer resistance to MI-2, CRISPR-Cas9 genetic screening was conducted in SK-Hep1 cells. The genome-wide CRISPR library was introduced into SK-Hep1 cells by lentiviral transduction. The T0 arm was used as one of the controls after puromycin selection. The cells were then divided into two groups with or without treatment of MI-2 (700 nM) for 45 d. The alterations in library representation were evaluated through Illumina deep sequencing to determine changes in gRNA abundance.

To explore the mechanisms underlying the synergistic lethality of sorafenib, kinase-based CRISPR screenings were performed in Hep3B and MHCC97H cells. The kinase CRISPR library was introduced into Hep3B and MHCC97H cells by lentiviral transduction. Cells with stable gRNA expression were cultured for 14

d. The abundance of gRNA was assessed by Illumina deep sequencing. For each sgRNA, the fold change in enrichment was calculated by comparing the T14 group (cultured for 14 d) with the T0 group.

**CellTitle-Blue Cell Viability Assay.** Cells were seeded into 96-well plates at a density of 2,000 to 2,500 cells per well and cultured in 100  $\mu$ L of medium containing the specified drugs for 4 to 5 d. CellTiter-Blue® Reagent (Cat# G8080, Promega) (20  $\mu$ L per well) was added into the assay plates and then incubated for 2 to 4 h. Fluorescence was recorded at 560/590 nm.

**Tissue Microarray and Scoring.** A tissue microarray consisting of 75 hepatocellular carcinoma (HCC) specimens was created using samples collected from patients who had undergone curative surgery at the Affiliated Eastern Hepatobiliary Hospital in Shanghai, China. Ethical approval was granted by the Eastern Hepatobiliary Hospital Research Ethics Committee, and written informed consent was obtained from each participating patient. The assembly of tissue microarrays, immunohistochemistry (IHC), and measurement of integrated optical density (IOD) were performed. Formalin-fixed paraffin-embedded tissue microarray was probed with the GPX4 antibody (Cat# ab125066, Abcam, 1:1,200 dilution) and MALT1 antibody (sc-46677, Santa Cruz Biotechnology, 1:50 dilution). An EnVision Detection kit (Cat# GK500705, Gene Tech, Shanghai, China) was utilized for the visualization of GPX4 and MALT1. For the measurement of IOD, the imaging system consisted of a Leica CCD camera DFC420 connected to a Leica DM IRE2 microscope (Leica Microsystems Imaging Solutions Ltd., Cambridge, UK). Photographs of representative fields were taken using the Leica QWin Plus v3 software at high-power magnification ( $\times 200$ ). Image-Pro Plus v6.0 software (Media Cybernetics, Inc., MD) was used to measure and count the IODs in each image.

**Generation of Liver Cancer Organoid.** Liver cancer tissues were minced and digested with PBS supplemented with collagenase type IV at 37 °C for 30 to 60 min. The suspension was filtered through a 100- $\mu$ m cell strainer and then centrifuged. The pellet was resuspended in cold organoid culture medium and then combined with Matrigel at a 1:2 ratio to achieve a cell density of 4,000 cells per 50  $\mu$ L before being seeded into a 12-well culture plate. Organoid culture medium was added to each well after solidification and organoids were cultured in a humidified incubator at 37 °C with 5% CO<sub>2</sub>. The organoids were then cultured for 5 to 7 d in medium supplemented with the specific drugs. Image acquisition was by means of ZEISS AxioObserver7. Image processing was conducted using ImageJ software.

**Immunohistochemical Staining.** Formalin-fixed paraffin-embedded samples were obtained from xenograft tumors and then probed with antibodies against GPX4 (Cat# ab125066, Abcam), Ki67 (Cat# ab16667, Abcam), 4-HNE (Cat# MAB3249, R&D), and caspase-3 (Cat# ab32351, Abcam). Following incubation

with the primary antibodies, positive cells were visualized using DAB+ as a chromogen.

**Statistics.** All the computational analyses and graphical visualization were performed with Prism 7 software (GraphPad). All *in vitro* data are reported as the mean  $\pm$  SD, and all *in vivo* data are presented as mean  $\pm$  SEM. Correlation between two continuous variables was measured by Pearson's r correlation. For the animal experiments, mice were randomly grouped before different treatments.

**Data, Materials, and Software Availability.** All study data are included in the article and/or [supporting information](#).

**ACKNOWLEDGMENTS.** This work was funded by grants from the National Natural Science Foundation of China (82473367, 82122047, 82072633, 82403136, 82330095, 81920108025, 82203044, 82003171, 82202062, and 82303000), Shanghai Pilot Program for Basic Research–Shanghai Jiao Tong University (21TQ1400225), Medical Engineering Interdisciplinary Program–Shanghai Jiao Tong University (24X010301470), Innovative research team of high-level local universities in Shanghai, Central University Outstanding Youth Team Cultivation Program, National Facility for Translational Medicine (TMSK-2021-129), Shanghai Municipal Education Commission–Gaofeng Clinical Medicine Grant Support (20181703), and Shanghai Natural Science Foundation (22ZR1480900 and 23YF1443400).

Author affiliations: <sup>a</sup>State Key Laboratory of Systems Medicine for Cancer, Shanghai Cancer Institute, Renji Hospital, Shanghai Jiao Tong University School of Medicine, Shanghai 200032, China; <sup>b</sup>German Cancer Research Center, Division Immune Regulation in Cancer, Heidelberg 69120, Germany; <sup>c</sup>Division of Reproduction and Genetics, First Affiliated Hospital of University of Science and Technology of China, Hefei National Research Center for Physical Sciences at the Microscale, University of Science and Technology of China, Hefei 230027, China; <sup>d</sup>Shanghai Immune Therapy Institute, Renji Hospital, Shanghai Jiao Tong University School of Medicine, Shanghai 200032, China; <sup>e</sup>Division of Molecular Oncology & Immunology, The Netherlands Cancer Institute, Amsterdam 1066 CX, The Netherlands; <sup>f</sup>Department of Medical Oncology, Shanghai Tenth People's Hospital, Tongji University, School of Medicine, Shanghai 200072, China; <sup>g</sup>National Research Center for Translational Medicine (Shanghai), State Key Laboratory of Medical Genomics, Ruijin Hospital, Shanghai Jiao Tong University School of Medicine, Shanghai 200025, China; <sup>h</sup>Department of Liver Surgery and Transplantation, Liver Cancer Institute, Zhongshan Hospital, Key Laboratory of Carcinogenesis and Cancer Invasion, Ministry of Education, Fudan University, Shanghai 200032, China; <sup>i</sup>Department of Interventional Radiology, Tongren Hospital, Shanghai Jiao Tong University School of Medicine, Shanghai 200336, China; <sup>j</sup>Institute of Translational Medicine, Zhangjiang Institute for Advanced Study, Shanghai Jiao Tong University, Shanghai 200240, China; and <sup>k</sup>Division of Molecular Carcinogenesis, OncoMed Institute, The Netherlands Cancer Institute, Amsterdam 1066 CX, The Netherlands

Author contributions: B.M., W.Q., C.S., R.B., and C.W. designed research; J.W., L.L., B.M., B.Y., B.L., X.M., A.F., S.W., J.H., Q.Z., S.J., G.J., J.Z., Y.C., and H.W. performed research; J.W., L.L., B.M., B.Y., B.L., X.M., A.F., S.W., J.H., Q.Z., S.J., G.J., J.Z., Y.C., H.W., C.S., and R.B. analyzed data; W.Q., C.S., R.B., and C.W. supervised research; and J.W., C.S., R.B., and C.W. wrote the paper.

1. S. J. Dixon *et al.*, Ferroptosis: An iron-dependent form of nonapoptotic cell death. *Cell* **149**, 1060–1072 (2012).
2. B. R. Stockwell *et al.*, Ferroptosis: A regulated cell death nexus linking metabolism, redox biology, and disease. *Cell* **171**, 273–285 (2017).
3. W. S. Yang *et al.*, Regulation of ferroptotic cancer cell death by GPX4. *Cell* **156**, 317–331 (2014).
4. G. Lei, L. Zhuang, B. Gan, Targeting ferroptosis as a vulnerability in cancer. *Nat. Rev. Cancer* **22**, 381–396 (2022).
5. V. S. Viswanathan *et al.*, Dependency of a therapy-resistant state of cancer cells on a lipid peroxidase pathway. *Nature* **547**, 453–457 (2017).
6. M. E. Wang *et al.*, RB1-deficient prostate tumor growth and metastasis are vulnerable to ferroptosis induction via the E2F/ACSL4 axis. *J. Clin. Invest.* **133**, e166647 (2023).
7. H. Liu *et al.*, Small-molecule allosteric inhibitors of GPX4. *Cell Chem. Biol.* **29**, 1680–1693.e1689 (2022).
8. B. R. Stockwell, Ferroptosis turns 10: Emerging mechanisms, physiological functions, and therapeutic applications. *Cell* **185**, 2401–2421 (2022).
9. A. Vogel, T. Meyer, G. Sapisochin, R. Salem, A. Saborowski, Hepatocellular carcinoma. *Lancet* **400**, 1345–1362 (2022).
10. H. Sung *et al.*, Global Cancer Statistics 2020: GLOBOCAN estimates of incidence and mortality worldwide for 36 cancers in 185 countries. *CA Cancer J. Clin.* **71**, 209–249 (2021).
11. Anonymous, EASL Clinical Practice Guidelines: Management of hepatocellular carcinoma. *J. Hepatol.* **69**, 182–236 (2018).
12. J. M. Llovet *et al.*, Sorafenib in advanced hepatocellular carcinoma. *N. Engl. J. Med.* **359**, 378–390 (2008).
13. M. Kudo *et al.*, Lenvatinib versus sorafenib in first-line treatment of patients with unresectable hepatocellular carcinoma: A randomised phase 3 non-inferiority trial. *Lancet* **391**, 1163–1173 (2018).
14. R. S. Finn *et al.*, Atezolizumab plus bevacizumab in unresectable hepatocellular carcinoma. *N. Engl. J. Med.* **382**, 1894–1905 (2020).
15. A. L. Cheng *et al.*, Updated efficacy and safety data from IMBrave150: Atezolizumab plus bevacizumab vs. sorafenib for unresectable hepatocellular carcinoma. *J. Hepatol.* **76**, 862–873 (2022).
16. Y. Du *et al.*, APE1 inhibition enhances ferroptotic cell death and contributes to hepatocellular carcinoma therapy. *Cell Death Differ.* **31**, 431–446 (2024).
17. C. Conche *et al.*, Combining ferroptosis induction with MDSC blockade renders primary tumours and metastases in liver sensitive to immune checkpoint blockade. *Gut* **72**, 1774–1782 (2023).
18. K. Wu *et al.*, Creatine kinase B suppresses ferroptosis by phosphorylating GPX4 through a moonlighting function. *Nat. Cell Biol.* **25**, 714–725 (2023).
19. Z. Zhang *et al.*, RNA-binding protein ZFP36/ITP protects against ferroptosis by regulating autophagy signaling pathway in hepatic stellate cells. *Autophagy* **16**, 1482–1505 (2020).
20. Z. Ye *et al.*, FBW7-NRA41-SCD1 axis synchronously regulates apoptosis and ferroptosis in pancreatic cancer cells. *Redox Biol.* **38**, 101807 (2021).
21. H. Akiyama *et al.*, Mitochondrial regulation of GPX4 inhibition-mediated ferroptosis in acute myeloid leukemia. *Leukemia* **38**, 729–740 (2024).
22. J. Hachmann, G. S. Salvesen, The Paracaspase MALT1. *Biochimie* **122**, 324–338 (2016).
23. K. M. Jeltsch *et al.*, Cleavage of roquin and regnase-1 by the paracaspase MALT1 releases their cooperatively repressed targets to promote T(H)17 differentiation. *Nat. Immunol.* **15**, 1079–1089 (2014).
24. C. G. Vinuesa *et al.*, A RING-type ubiquitin ligase family member required to repress follicular helper T cells and autoimmunity. *Nature* **435**, 452–458 (2005).
25. O. Zhang *et al.*, New insights into the RNA-binding and E3 ubiquitin ligase activities of roquins. *Sci. Rep.* **5**, 15660 (2015).
26. L. Fontan *et al.*, MALT1 small molecule inhibitors specifically suppress ABC-DLBCL in vitro and in vivo. *Cancer Cell* **22**, 812–824 (2012).
27. B. Yan *et al.*, Pharmacological inhibition of MALT1 (mucosa-associated lymphoid tissue lymphoma translocation protein 1) induces ferroptosis in vascular smooth muscle cells. *Cell Death Discov.* **9**, 456 (2023).
28. M. J. Hangauer *et al.*, Drug-tolerant persister cancer cells are vulnerable to GPX4 inhibition. *Nature* **551**, 247–250 (2017).

29. J. Bruix *et al.*, Regorafenib for patients with hepatocellular carcinoma who progressed on sorafenib treatment (RESOURCE): A randomised, double-blind, placebo-controlled, phase 3 trial. *Lancet* **389**, 56–66 (2017).
30. B. I. Carr *et al.*, Fluoro-Sorafenib (Regorafenib) effects on hepatoma cells: Growth inhibition, quiescence, and recovery. *J. Cell Physiol.* **228**, 292–297 (2013).
31. S. J. Dixon *et al.*, Pharmacological inhibition of cystine–glutamate exchange induces endoplasmic reticulum stress and ferroptosis. *eLife* **3**, e02523 (2014).
32. R. Gao *et al.*, YAP/TAZ and ATF4 drive resistance to Sorafenib in hepatocellular carcinoma by preventing ferroptosis. *EMBO Mol. Med.* **13**, e14351 (2021).
33. W. Huang *et al.*, ABCC5 facilitates the acquired resistance of sorafenib through the inhibition of SLC7A11-induced ferroptosis in hepatocellular carcinoma. *Neoplasia* **23**, 1227–1239 (2021).
34. L. Wang *et al.*, ATF3 promotes erastin-induced ferroptosis by suppressing system Xc(. *Cell Death Differ.* **27**, 662–675 (2020).
35. P. Koppula, L. Zhuang, B. Gan, Cystine transporter SLC7A11/xCT in cancer: Ferroptosis, nutrient dependency, and cancer therapy. *Protein Cell* **12**, 599–620 (2021).
36. M. S. Brose *et al.*, Sorafenib in radioactive iodine-refractory, locally advanced or metastatic differentiated thyroid cancer: A randomised, double-blind, phase 3 trial. *Lancet* **384**, 319–328 (2014).
37. A. Grothey *et al.*, Regorafenib monotherapy for previously treated metastatic colorectal cancer (CORRECT): An international, multicentre, randomised, placebo-controlled, phase 3 trial. *Lancet* **381**, 303–312 (2013).
38. X. Han *et al.*, ZEB1 directly inhibits GPX4 transcription contributing to ROS accumulation in breast cancer cells. *Breast Cancer Res. Treat.* **188**, 329–342 (2021).
39. L. K. Chu *et al.*, Autophagy of OTUD5 destabilizes GPX4 to confer ferroptosis-dependent kidney injury. *Nat. Commun.* **14**, 8393 (2023).
40. L. Liu *et al.*, Deubiquitinase OTUD5 as a novel protector against 4-HNE-triggered ferroptosis in myocardial ischemia/reperfusion injury. *Adv. Sci. (Weinh)* **10**, e2301852 (2023).
41. J. Li *et al.*, Tumor-specific GPX4 degradation enhances ferroptosis-initiated antitumor immune response in mouse models of pancreatic cancer. *Sci. Transl. Med.* **15**, eadg3049 (2023).
42. K. Martin *et al.*, Pharmacological inhibition of MALT1 protease leads to a progressive iPEx-like pathology. *Front. Immunol.* **11**, 745 (2020).
43. S. Biswas *et al.*, Pharmacological inhibition of MALT1 ameliorates autoimmune pathogenesis and can be uncoupled from effects on regulatory T-cells. *Front. Immunol.* **13**, 875320 (2022).
44. L. Sun, L. Deng, C. K. Ea, Z. P. Xia, Z. J. Chen, The TRAF6 ubiquitin ligase and TAK1 kinase mediate IKK activation by BCL10 and MALT1 in T lymphocytes. *Mol. Cell* **14**, 289–301 (2004).
45. M. Minderman *et al.*, MALT1-dependent cleavage of CYLD promotes NF- $\kappa$ B signaling and growth of aggressive B-cell receptor-dependent lymphomas. *Blood Cancer J.* **13**, 37 (2023).
46. A. Schmitt *et al.*, BRD4 inhibition sensitizes diffuse large B-cell lymphoma cells to ferroptosis. *Blood* **142**, 1143–1155 (2023).
47. C. Zheng *et al.*, Donafenib and GSK-J4 synergistically induce ferroptosis in liver cancer by upregulating HMOX1 expression. *Adv. Sci. (Weinh)* **10**, e2206798 (2023).
48. J. Rodenca *et al.*, Sensitization of cancer cells to ferroptosis coincident with cell cycle arrest. *Cell Chem. Biol.* **31**, 234–248.e13 (2023), 10.1016/j.chembiol.2023.10.011.
49. S. Yuan *et al.*, Sorafenib attenuates liver fibrosis by triggering hepatic stellate cell ferroptosis via HIF-1 $\alpha$ /SLC7A11 pathway. *Cell Proliferation* **55**, e13158 (2022).